

Electrochemically Induced Film Formation on CoCrMo Alloy for Hip Implant Application

S. Kerwell¹ · D. Baer² · E. Martin³ · Y. Liao³ · M. A. Wimmer² · K. Shull³ · M. T. Mathew^{2,4}

Received: 29 June 2016/Revised: 31 October 2016/Accepted: 2 November 2016/Published online: 15 November 2016
© Springer International Publishing Switzerland 2016

Abstract Metal-on-metal (MoM) hip retrievals exhibited the presence of carbonaceous tribofilms, derived from synovial proteins, particularly on the articulating surfaces. Studies suggest that the films decrease corrosion and wear. To extend implant longevity and minimize the side effects due to released metal ions/debris, it is important to investigate the possibility of generating such films artificially on the implant surfaces (before implantation) and evaluate its corrosion resistance in a simulated hip environment. Hence, in this study, a film that mimics tribolayer is generated on CoCrMo alloy surface through electrochemical treatment. The mechanism of formation and corrosion resistance is evaluated by electrochemical impedance spectroscopy (EIS) technique. A standard three-electrode

corrosion cell was used to conduct the experiments on polished ($R_a < 10.0$ nm) CoCrMo alloy disks in bovine calf serum with three different protein concentrations (0, 15, and 30 g/L) and at four different treatment potentials (−0.4, +0.6, +0.7, and +0.8 V). EIS testing (at E_{oc} , potential amplitude: ± 10 mV, frequency range 100 kHz to 0.005 Hz) was conducted pre- and post-potentiostatic treatment. Tribofilm was evaluated by scanning electron microscopy, white light interferometry, and Raman spectroscopy. Results suggest evidence of electrochemically induced film formation and their potential ability to increase the corrosion resistance of biomedical implants.

✉ M. T. Mathew
mtmathew@uic.edu

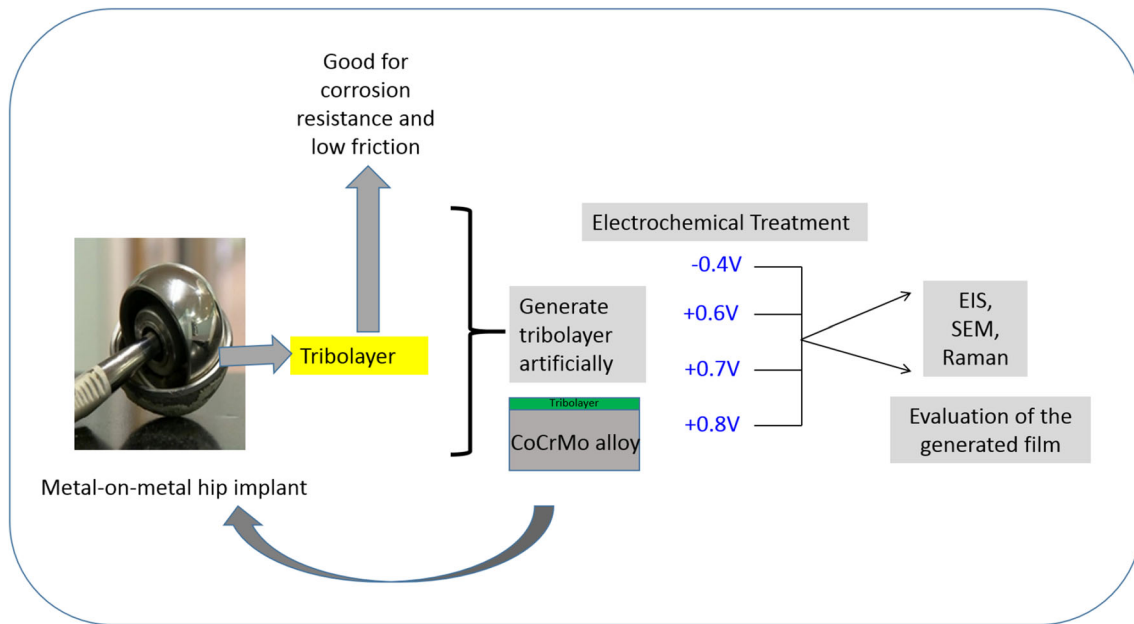
¹ Department of Bioengineering, University of Illinois at Chicago, Chicago, IL, USA

² Orthopedic Surgery, Rush University Medical Center, Chicago, IL, USA

³ Department of Materials Science and Engineering, Northwestern University, Evanston, IL, USA

⁴ Department of Biomedical Science, UIC School of Medicine at Rockford, Rockford, IL, USA

Graphical Abstract



Keywords Cobalt–chromium–molybdenum alloy (CoCrMo) · Electrochemical impedance spectroscopy · Corrosion · Wear · Protein · Orthopedic implants

1 Introduction

Total hip replacement (THR) surgery is an increasingly popular treatment for the management of hip arthritis in elderly patients and individuals who suffer from degenerative joint disease [1]. By the year 2030, the total number of hip replacement procedures performed within the US is projected to increase to 572,000, a 174% growth compared to the 208,600 number of procedures performed in 2005 [2]. In addition to elderly THR patients, there exists a cohort of THR patients who are younger, active, and have longer life expectancies [3]. Benefits of a THR include an increased quality of life among patients, allowing them to live with improved mobility and pain relief.

The choice of implant bearing type depends on the lifestyle of the patient [4]. For younger patients, ceramic-on-ceramic (CoC) and metal-on-metal (MoM) surfaces are still considered because they can withstand the increased loads on the implant [4–6]. MoM THRs, made of CoCrMo alloys, demonstrate biocompatibility, high corrosion resistance, and wear properties [7–10]. Although MoM THR implants do provide a solution to hip arthritis, concerns about the devices have grown and since 2009, these implants have been excluded from the US implant market. The problems/concerns with hip implants include wear, which is material loss due to friction [11] and corrosion,

the chemical degradation of materials [12]. The synergy between wear and corrosion processes on material degradation is termed tribocorrosion [13]. Hence, identifying a potential solution to such issues is an attractive research topic among the biomedical researchers.

Recent studies showed that proteins within the synovial fluid surrounding the joint implants affect the corrosion kinetics of MoM implants. However, the interaction between proteins and the implant surface has not been thoroughly investigated [14, 15]. It has been reported that synovial joint proteins, which are largely plasma proteins, are able to form a protective layer on the surface of the implant that helps to limit the wear [8, 11, 13, 16–18]. These films are termed tribofilms or tribochemical reaction layers, and were identified on retrieved implants and mechanically tested CoCrMo alloy surfaces using hip simulators [17].

Wimmer et al. [18] conducted surface analyzes of MoM hip retrievals, and found that at least eighty percent of the retrieved femoral bearing heads or acetabular cups displayed tribochemical layers. The layers, when present, were predominantly located near to the articulating surfaces of the THR bearing [18]. X-ray photoelectron spectroscopy analysis (XPS) indicated that the tribochemical reaction layers largely consisted of decomposed organic proteins and salts that were deposited onto oxide layers located on the metal surfaces [18]. Liao et al. [19] studied the tribofilms on hip retrievals with Raman spectroscopy, and identified two Raman shifts that are signature to graphitic carbon. The presence of graphene within the tribofilm could help to reduce wear and corrosion at the

implant surface by acting as a solid lubricant [19], but could also cause biocompatibility issues. Wear processes may lead to dispersion of graphitic fragments into the pseudo-synovial fluid, presenting challenges in systemic transport.

In 2013, Martin et al. [20] found that carbonaceous films will form on CoCrMo thin films when the alloy is corroded in bovine calf serum using potentiodynamic scans, and the film deposition was measured at the alloy surface at potentials near +0.77 V versus SCE (Standard calomel electrode). The films also formed on pure molybdenum thin films during potentiodynamic tests at potentials near +0.06 V versus SCE, but not on the pure Co and Cr surfaces, suggesting that molybdenum is necessary to initiate the film formation [20]. X-ray photoelectron spectroscopy (XPS) analysis confirmed that the films are derived from the serum proteins because the nitrogen was found in the amide or amine states and the nitrogen–carbon ratio was the same as that of serum proteins, including albumin [9, 15].

As a result of the findings by Martin et al. [20] the goal of this study was to induce film formation on CoCrMo surfaces in a proteinaceous environment through electrochemical treatment of the metal, and then evaluate the film's effectiveness in resisting corrosion through electrochemical impedance spectroscopy (EIS). To extend implant longevity and minimize the side effects due to released metal ions/debris, it is important to investigate the possibility of generating such films artificially on the implant surfaces (before implantation) and evaluate its corrosion resistance in a simulated hip environment. We hypothesized that (1) carbonaceous film formation is influenced by the electrochemical potential and by protein content and that (2) at high protein concentrations, the films will promote superior corrosion resistance than films formed from solutions with lower protein concentrations.

2 Materials and Methods

2.1 Sample Preparation

In this study, 24 high-carbon (HC-wrought) CoCrMo alloy disks of 12 mm diameter and 3 mm thickness supplied by ATI Alvac Inc. (Pittsburgh, PA 15222, USA) were used. Table 1 shows the chemical composition of the disk samples. All samples were mechanically polished to a mirror

surface finish ($R_a < 10.0$ nm). Prior to each experiment, the sample was cleaned ultrasonically in 70% isopropyl alcohol for 10 min and then in distilled water for 10 min. **Electrochemical treatment** In 2011, our group showed that CoCrMo corrosion kinetics is improved in the presence of a specific protein concentration range because of superior passive film generation on the alloy surface [17–19]. Potentiodynamic curves of the CoCrMo alloy in the tested electrolytes (as a function of protein concentration) from that study are shown in Fig. 1. These data helped to determine the treatment potentials and the various electrolyte compositions to use during the electrochemical treatment in the present investigation.

Electrochemical testing was conducted with a standard three-electrode corrosion cell. A schematic figure of the set-up is seen in Fig. 2. CoCrMo alloy disks were used as the working electrodes (WE) with an exposed surface area of 0.385 cm^2 (The possibility of interstitial corrosion with o'ring is not considered in the analysis). The counter electrode was a graphite rod and the reference electrode was a saturated calomel electrode (SCE). 10 mL of the electrolyte was used for each sample and was pre-warmed to 37°C (physiological temperature) prior to testing. During the tests, the fluid was maintained at this temperature using a water bath. The electrolyte was simulated synovial fluid, the composition of which is provided in Table 2.

The experimental design of the two series of electrochemical tests is described in Fig. 3. The first series of tests was designed to gather corrosion mechanism-related information on film formation. Therefore, the EIS tests and the potentiostatic polarization step were all conducted at the same treatment potential. The second series of experiments was designed to determine film stability and clinical relevance. Therefore, the EIS experiments were conducted at Eoc before and after the potentiostatic treatment step.

The same treatment potentials and electrolyte concentrations were used in both sets of tests. Four treatment potentials were tested: -0.4 , $+0.6$, $+0.7$, and $+0.8$ V. The values of $+0.6$, $+0.7$, and $+0.8$ V were chosen to examine the repassivation regime while the value of -0.4 V was chosen as a control and corresponds to the period of film passivation. Protein concentration in the electrolyte solution was also varied between tests. Three protein concentrations were tested: 0, 15, and 30 g/L. These values correspond to (1) the normal physiological value, 15 g/L,

Table 1 Composition of CoCrMo alloy

Disk dimensions (mm)	High-carbon CoCrMo alloy chemical composition (wt%)							
	Thickness	C	Co	Cr	Mo	Si	Mn	Al
Diameter								
12	3	0.034	64.96	27.56	5.70	0.38	0.60	<0.02

Fig. 1 Potentiodynamic test of CoCrMo in various concentrations of electrolyte. The graph shows the transpassive region (+0.6 to 0.8), where the current is decreased, indicating the possible film formation

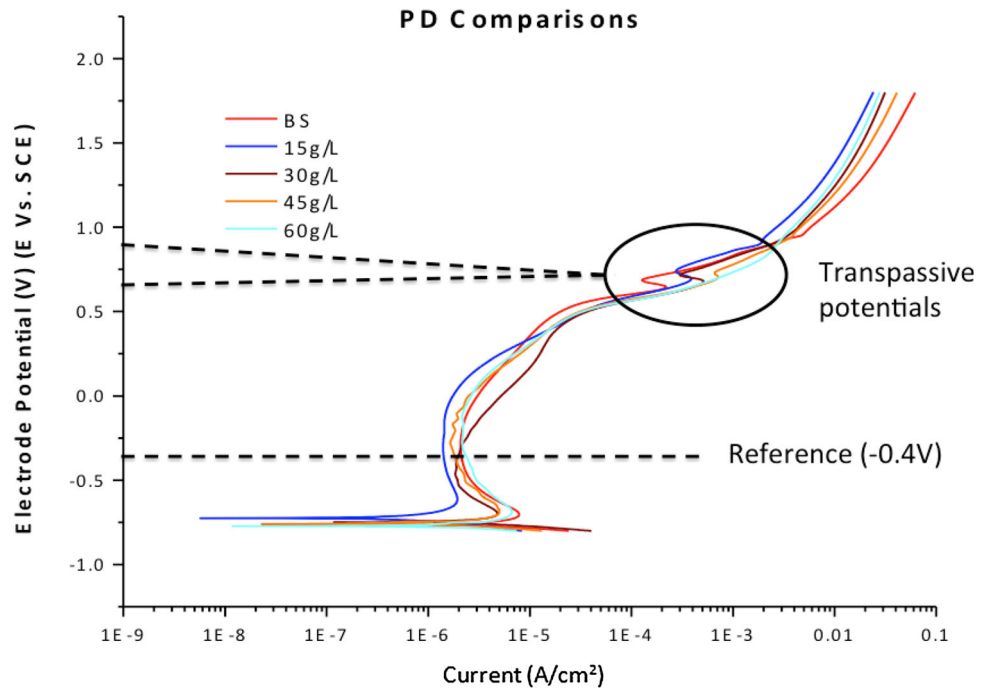
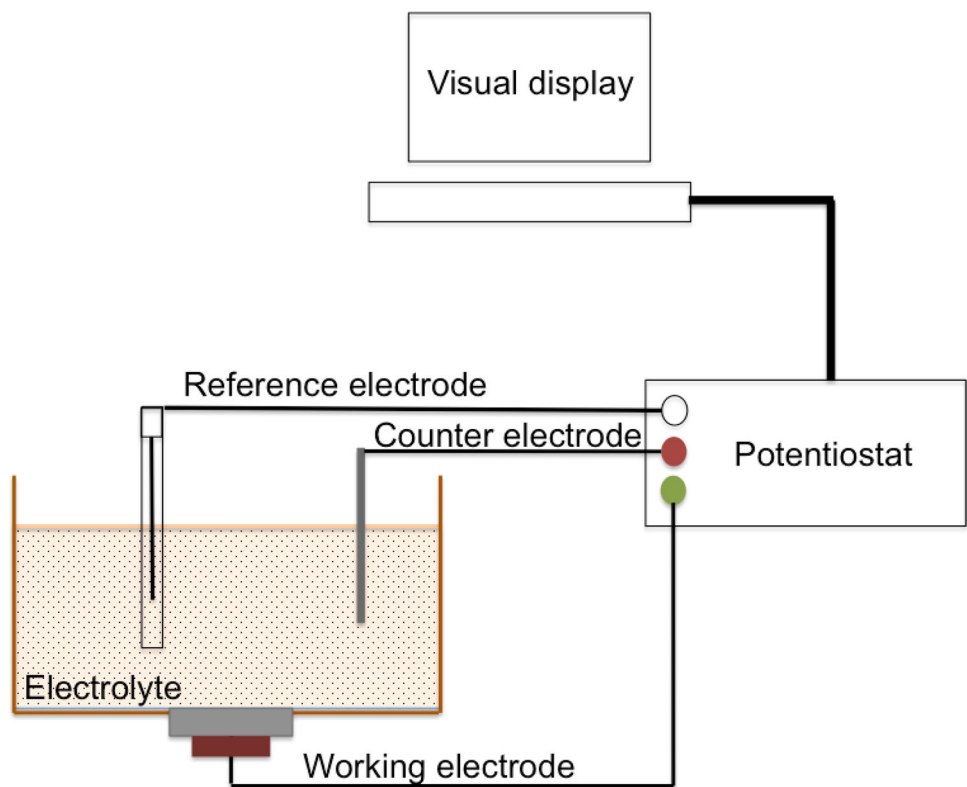


Fig. 2 Schematic diagram of the standard three-electrode corrosion cell used in electrochemical testing. The reference electrode (RE), a counter electrode (CE), and working electrode (WE—the specimen) is connected to the potentiostat



(2) values due to inflammation, 30 g/L, and (3) a control value of 0 g/L protein content [21]. Three tests were conducted at each variable experimental condition ($N = 3$).

The entire electrochemical test consisted of six steps, as explained in Fig. 4:

1. OCP 1: The open circuit potential at the WE was measured for 3 min to ensure that all electrical connections were set up correctly.
2. OCP 2: The OCP was measured for 30 min as the corrosion cell stabilized.

Table 2 Composition of bovine calf serum (BCS) electrolyte

NaCl (g/L)	EDTA (g/L)	Tris (g/L)	Protein (g/L)
<i>Composition of bovine calf serum (BCS) electrolyte</i>			
9	0.2	27	30

3. EIS 1: EIS testing (potential treatment, potential amplitude: ± 10 mV, frequency range 100 kHz–0.005 Hz) was conducted to measure the properties of the material surface before each treatment step.

4. Treatment step (potentiostatic polarization): A specific potential (-0.4 , $+0.6$, $+0.7$, or $+0.8$ V) was applied to the surface for 1 h to possibly induce film formation.
5. EIS 2: EIS tests were repeated on the specimen to measure the effects of the treatment potential on the material’s corrosion kinetics.
6. OCP 3: The OCP was measured again to determine if this value changed following electrochemical treatment.

In the first series of tests, the EIS steps were conducted at the same potential as the potentiostatic polarization step

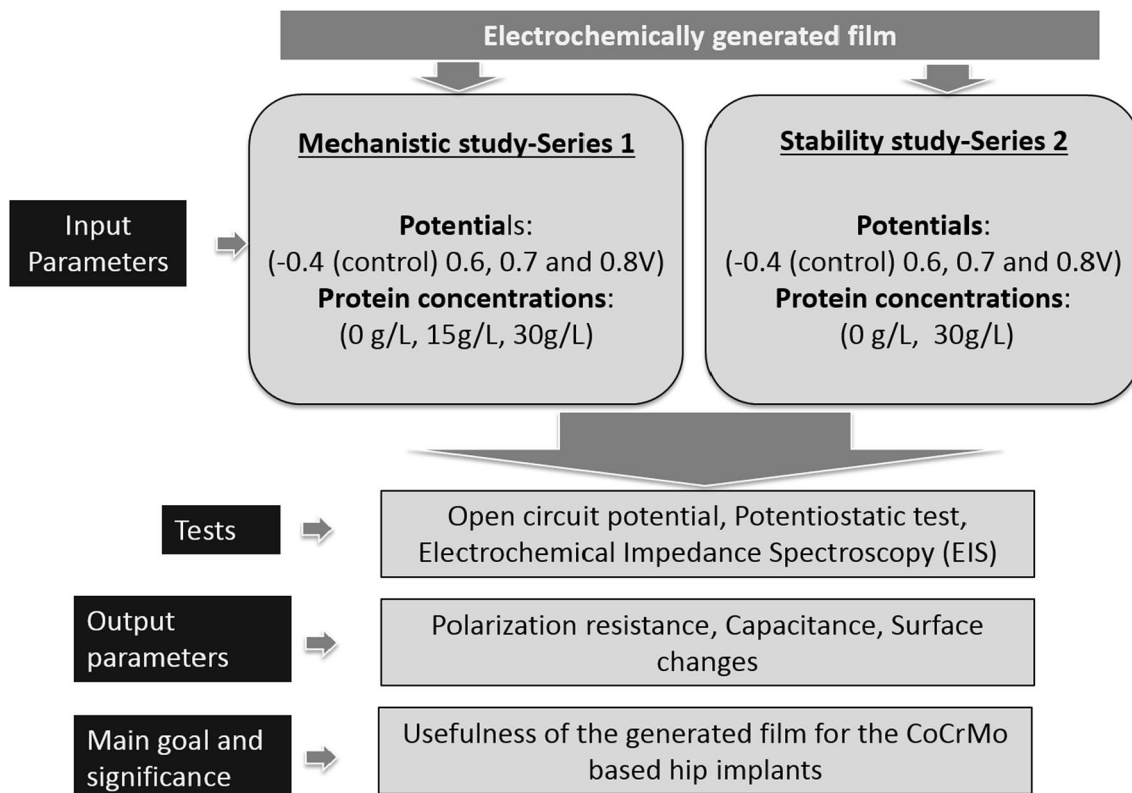
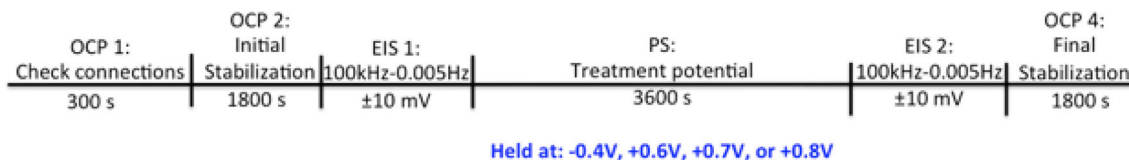


Fig. 3 Schematic of the testing parameters used in the study, protein concentration, and electrochemical potentials. The study is divided into two series: series 1: mechanistic study and series 2: electrochemical stability of the film at clinically relevant conditions



Series 1: EIS 1 and 2 at the potential of the treatment (-0.4 , $+0.6$, $+0.7$, $+0.8$)

Series 2: EIS 1 and 2 at the free potential (E_{oc})

Fig. 4 The electrochemical protocol used in the study. The differences between the two series are that series 1 was designed to understand the mechanistic information behind film formation while series 2 was designed to measure the electrochemical stability of the film

(Step 5). In the second set of tests, EIS tests were conducted at E_{oc} .

After each experiment, the WE specimen was sonicated for 15 min in 70% isopropyl alcohol and then in distilled water for 10 min.

2.2 Surface Characterization

Following electrochemical testing, white Light Interferometry (WLI) (Zygo New View 6300, Zygo Corporation, Middlefield, CT, USA) was conducted on three regions of each sample to determine surface roughness. The surfaces were then imaged using Scanning Electron Microscopy (SEM) (Jeol JSM-6490 LV, Oxford Instruments, Oxford, UK), and Energy dispersive X-ray spectroscopy (EDS) to observe the alloy microstructure and film composition. Raman Spectroscopy (Action Trivista CRS Confocal Raman System, NUANCE, Evanston, IL, USA) with excitation radiation of an Ar–Kr 514.5 nm gas laser at –10 mW was also performed on sample surfaces to quantify the carbon profile generated at each treatment potential.

3 Results

3.1 Electrochemical Treatment

The current evolution during the potentiostatic treatment step (Step 5) in 30 g/L protein content electrolytes is shown in Figs. 5. The result shows that, the current evolved at +0.6 V was greater than at +0.7 V. Current evolution is an indication of metal ion release, where K_c , the mass of metal ions released, is quantified by Faraday’s law:

$$K_c = \frac{Q \times M}{n \times F}, \tag{1}$$

where ‘ Q ’ is the anodic charge in coulombs (C) passed through the working electrode, determined by integrating the current over time, ‘ M ’ (g/mol) is the equivalent weight of the elements dissolved, ‘ n ’ is the dissolution valence (note that ‘ n ’ can be varied with applied potential), and ‘ F ’ is the Faraday’s constant (96485 C/mol.). Generally, increasing anodic potentials leads to increment in the current evolution.

3.2 Electrochemical Impedance Spectroscopy (EIS)

3.2.1 EIS of Series 1: Mechanistic Understanding of the Film Formation

As mentioned earlier, by doing EIS at a treatment potential, the mechanistic understanding of the film formation can be investigated. The after treatment Bode and Nyquist plots of Series 1 are presented in Fig. 6. Figure 6a, b show the Bode and Nyquist plots obtained at –0.4 V. The Nyquist plots are quarter circles, regardless of the protein content. The Bode phase angle plot displays one time constant, in which the results for all electrolyte concentrations closely overlap from low- to high-frequency values. Figure 6c, which shows the Bode plot at +0.6 V, demonstrates that higher impedances were obtained with increasing protein content of the electrolyte. The Nyquist plot of +0.6 V, in Fig. 6d, resulted in semi-circles with a loop, which show reduced corrosion kinetics with increasing protein content. The Bode phase angle plot of +0.7 V (Fig. 6e), shows two time constants, at low and high frequencies, for all protein content conditions. The plots are not overlapping at these

Fig. 5 Evolution of current during the electrochemical treatment at two protein concentrations 30 g/L. The current evolution during the potentiostatic treatment steps at all the potential parameters under consideration. The surrounding electrolyte was 30 g/L protein content

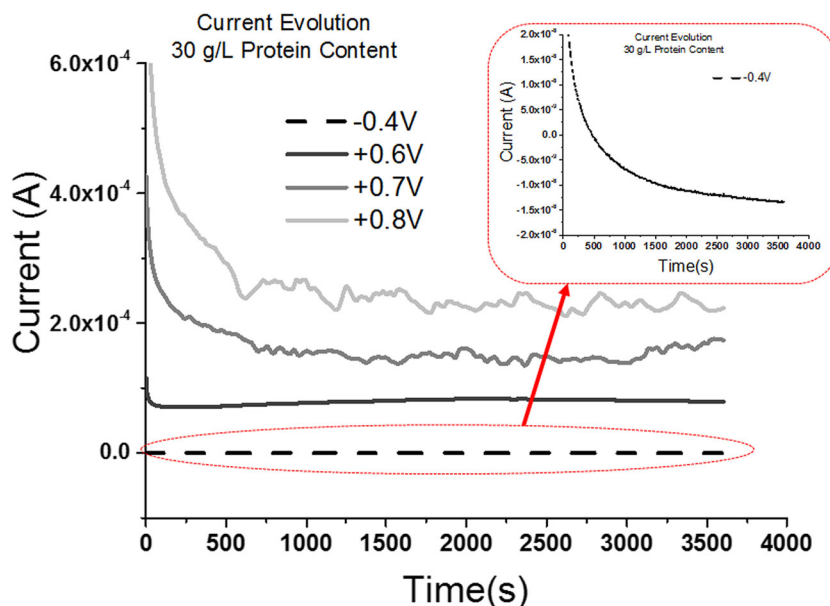
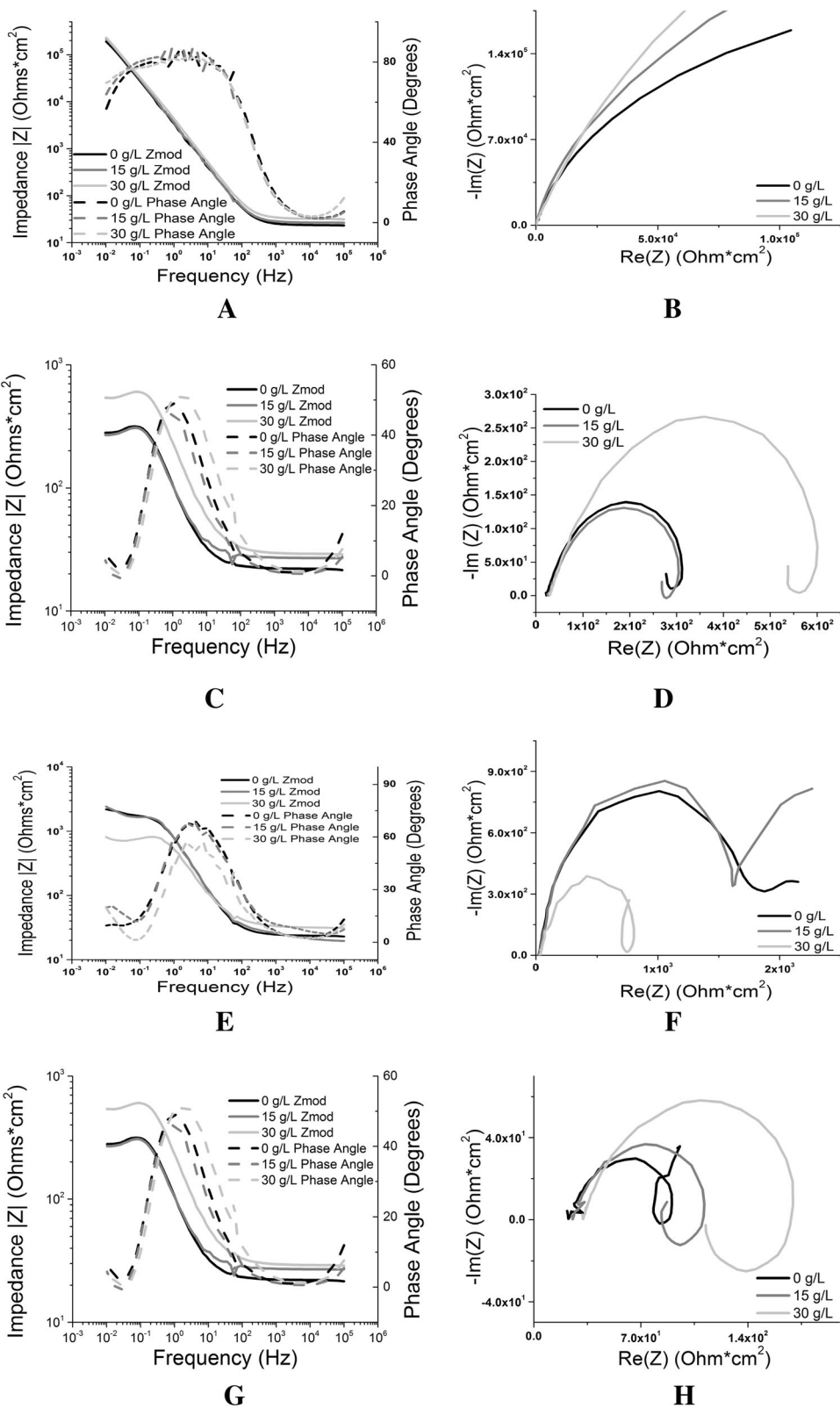


Fig. 6 a–h EIS at treated potential (series 1) **a** Bode and Nyquist plots as a function of treatment potential. **a** -0.4 V Bode plot, **b** -0.4 V Nyquist plot, **c** $+0.6$ V Bode Plot, **d** $+0.6$ V Nyquist Plot, **e** $+0.7$ V Bode Plot, **f** $+0.7$ V Nyquist Plot, **g** $+0.8$ V Bode Plot, **h** $+0.8$ V Nyquist Plot



values. The Nyquist plot of $+0.7$ V in Fig. 6f shows a loop associated with 30 g/L protein content while 0 and 15 g/L protein content conditions do not result in such a loop.

These results suggest that 15 g/L protein displays superior corrosion kinetics than other electrolyte conditions. The Bode phase angle plot for $+0.8$ V in Fig. 6g reveals two

time constants located at high- and low-frequency values, with 30 g/L protein resulting in superior anti-corrosion kinetics than other electrolyte conditions. In the Nyquist plot for +0.8 V (Fig. 6h), 30 g/L results in superior anti-corrosion kinetics. However, 0 g/L protein resulted in a full loop. The combination of +0.7 V with 15 g/L protein resulted in the most superior corrosion kinetics based on the Nyquist plot compared to +0.6 and +0.8 V. However, treatment at -0.4 V resulted in even greater corrosion resistance than at +0.7 V. The treatment at -0.4 V is within the natural passivation regime of CoCrMo, which explains its superior corrosion resistance.

3.2.2 EIS of Series 2: Stability of the Film in Clinically Relevant Conditions

As with Series 1 (Fig. 6), Fig. 7 displays the Bode and Nyquist plots for Series 2. In Fig. 7a, the Bode plot for -0.4 V shows a broader bandwidth occurring with 30 g/L protein, indicating superior film formation than 0 g/L protein. In Fig. 7b, the Nyquist plot for -0.4 V indicates a greater resistance to corrosion with the 30 g/L protein. There are two time constants shown in the +0.6 V Nyquist plot in Fig. 7c. The first one occurs at a lower frequency while the second one occurs at a mid-range frequency. However, both electrolyte conditions for +0.6 V appear to overlap throughout the frequency range. Similar to the results in Fig. 7b, in Fig. 7d, 30 g/L protein appears to have superior corrosion resistance than 0 g/L. In Fig. 7e, both 15 and 30 g/L protein show overlapping plots, while 0 g/L protein content shows less ability for film formation. In Fig. 7f, the Nyquist plot for +0.7 V shows that 30 g/L protein results in anti-corrosion kinetics than the plots for the other electrolyte conditions. The Bode plot of +0.8 V, shown in Fig. 7g, displays two time constants. The first one is located at a low frequency and the second one at mid-range frequencies; both of the electrolyte conditions resulted in separate curves, which only overlap towards higher frequencies. The Nyquist plot shown in Fig. 7h of +0.8 V, shows that the 0 g/L protein content electrolyte condition shows superior corrosion kinetics than the electrolyte, which has protein. To summarize Fig. 7, superior anti-corrosion kinetics was demonstrated with +0.7 V. Therefore, from both of these Series, +0.7 V shows promising evidence for being an optimum treatment potential for electrochemically induced film formation.

3.2.3 Equivalent Circuit Model

EIS data can be fit to an equivalent circuit model. Although such circuits do not correspond exactly to the complexity of an implant surface, they do provide the opportunity to model the general behavior of a specific metal and its

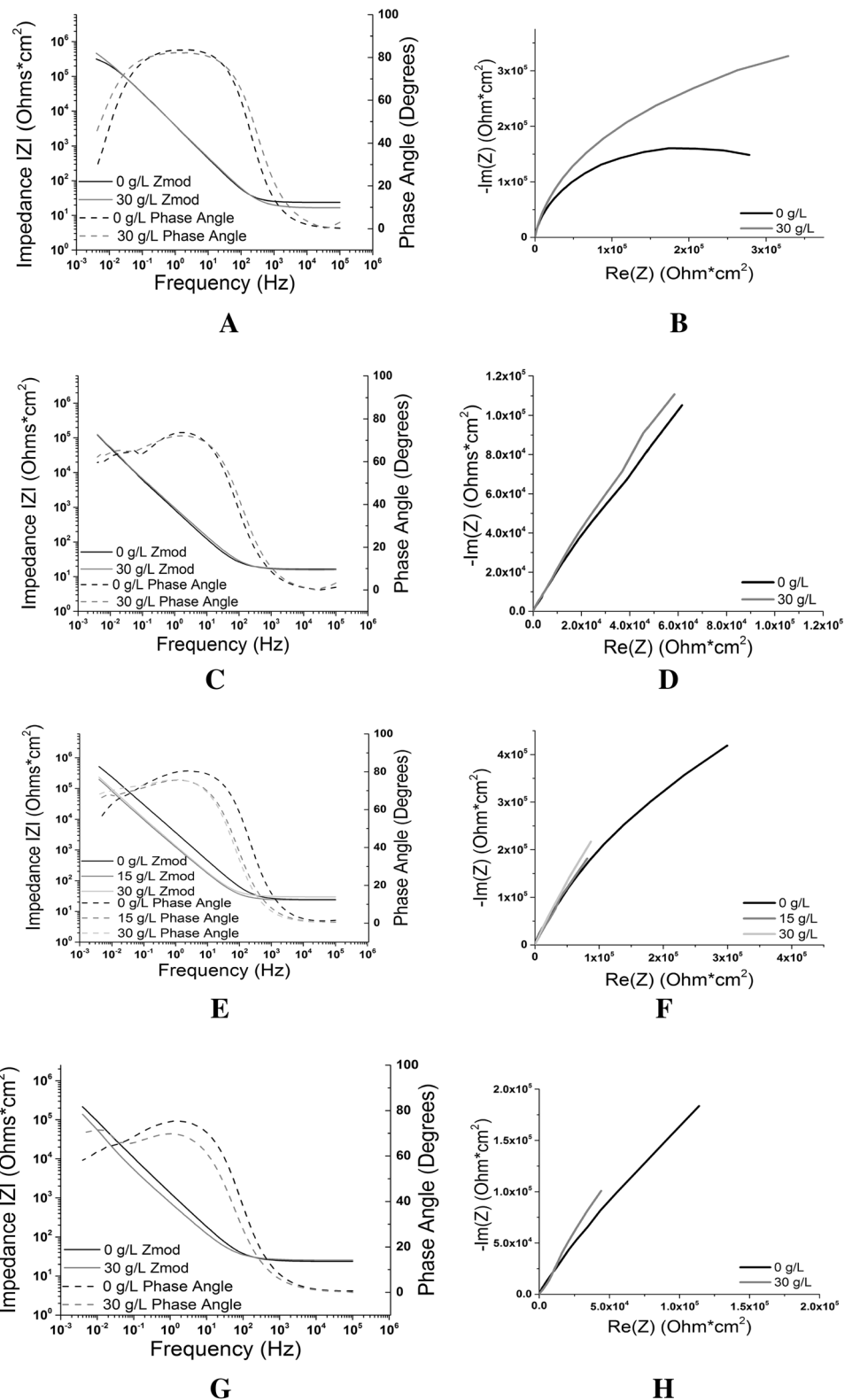
interface with surrounding conditions. Data from an equivalent circuit model can quantify the material's polarization resistance (R_p) and double layer capacitance (C_f). The simplest equivalent circuit is Randle's circuit. It is composed of a resistor in series with a resistor and capacitor that are in parallel. The first resistor corresponds to the resistance of the electrolyte that surrounds the alloy while the other two components correspond to the resistance and capacitance of the double layer that forms on top of the metal surface. These values reflect the bulk metal's resistance to corrosion. The higher the double layer resistance and the lower the double layer capacitance, the more resistant the surface is to corrosion. Since Randle's circuit is the simplest circuit model, it is not able to explain the complex behavior of the CoCrMo interface in an electrolyte. Therefore, a Randle's circuit modified with a constant phase element (CPE) was used in place of the capacitance of the double layer in the original Randle's circuit. Figure 8a shows the equivalent circuit that was used to model the experiments in Series 1. Because of strong loop-like behavior exhibited in the Nyquist plots for Series 1 (shown in Fig. 6), an inductor (L) was also incorporated into the model circuit of Series 1. It should be noted that, in Series 1, EIS data are from the surfaces with electrochemically active surfaces (EIS at treatment potential). Hence, additional series Part (R and C) together with inductance (L) represents the active electrochemical double layer, which consists of metal ion and active proteins. The reported R value is the summation of the resistances that are connected in series. ($R_{total} = R_{out} + R + R_{in}$).

Figure 8b shows the equivalent circuit that was used to model the experimental data for Series 2. The Chi squared value was in good agreement with experimental values (≤ 0.002) for each test using the respective equivalent circuit models.

During passivation, an oxide layer forms on the CoCrMo surface, greatly protecting it from corrosion. However, this oxide layer can be destroyed by mechanical wear. Therefore, this potential cannot serve as a long-term treatment for the implant. The potential of +0.7 V occurs during the repassivation regime, while +0.6 and +0.8 V occur before and after the repassivation regime, respectively. During repassivation, a carbonaceous film begins to reform on the metal surface. The evolution of polarization resistance and capacitance are shown in Fig. 9a, b for Series 1 and Fig. 9c, d for Series 2 using the respective equivalent circuits in Fig. 8a, b.

In Fig. 9a the resistance is highest using +0.7 V of the treatment potential as compared to the other potentials, although -0.4 V has the highest resistance for all concentrations, this potential is the potential where passivation of the film occurs, therefore resulting in the highest resistance because the passivation which occurs is a stronger

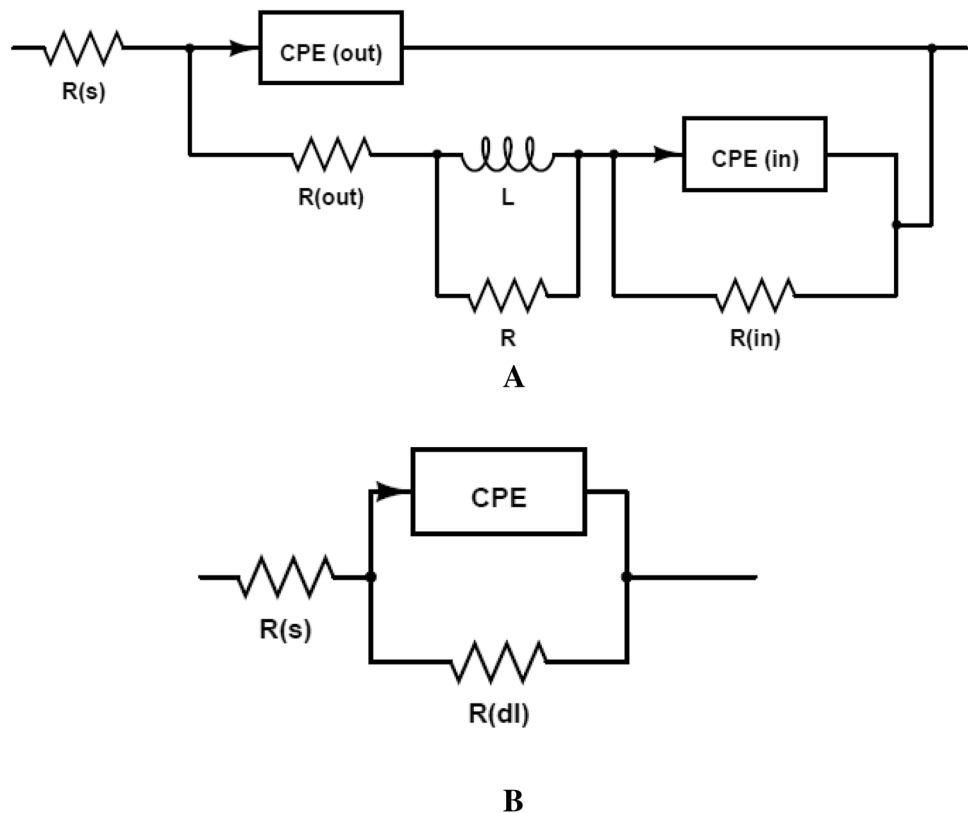
Fig. 7 EIS at Eoc (free potential-series 2) Bode and Nyquist plot as a function of treatment potential. **a** -0.4 Bode Plot, **b** -0.4 Nyquist Plot, **c** $+0.6$ V Bode Plot, **d** $+0.6$ V Nyquist Plot, **e** $+0.7$ V Bode Plot, **f** $+0.7$ V Nyquist Plot, **g** $+0.8$ V Bode Plot, **h** $+0.8$ V Nyquist Plot



film than that occurring during the repassivation regime (i.e., $+0.7$ V). The lowest resistance to corrosion was shown in the $+0.8$ V treatment potential throughout all the concentrations tested. In Fig. 9b, the capacitance after the

treatment is shown for each of the treatment potentials in each electrolyte condition. Throughout, $+0.6$ V displays the highest capacitance, which is due to CoCrMo having a pitting potential of $+0.6$ V. Therefore, this treatment

Fig. 8 a, b Equivalent circuits used for the EIS analysis are provided. For the mechanistic study (series 1) the circuit A is used. EIS was conducted at treated potential. R_s solution resistance, CPE_{out} constant phase element (*outer layer*), CPE_{in} constant phase element (*for inner layer*), L inductance, R resistance. In series 2, the circuit was quite simple, consisting of R_s solution resistance, CPE constant phase element, R_{dl} resistance of double layer. A CPE component will provide the capacitance of double layer. **a** Series 1 equivalent circuit, **b** series 2 equivalent circuit



potential had the highest capacitance as compared to any other treatment potential in the study. Again, +0.7 V demonstrates superior corrosion kinetics, as the capacitance is lower as compared to +0.6 or +0.8 V. Although, EIS results at -0.4 V demonstrate better corrosion kinetics than at +0.7 V, which indicates that the film during the passivation regime is stronger than the one occurring during the repassivation regime.

In Fig. 9c the resistance, R_p , after each treatment step at each potential is shown. As higher resistance is indicative of a superior resistance to corrosion, the +0.7 V has superior resistance as compared to other treatment potentials in either 0 or 30 g/L protein. We believe that a reason for this is that the potential of +0.7 V occurs in the repassivation range based on the CoCrMo potentiodynamic curve seen in the primary study with various protein concentrations. The results showed that the +0.7 V potential has the ability to induce proteinaceous film formation on CoCrMo surface.

The opposite behavior is observed in Fig. 9d, which shows the capacitance after each treatment step at each potential. As a higher capacitance corresponds to a decrease in corrosion resistance, metal surfaces exposed to +0.6 and +0.8 V show a greater tendency to undergo corrosion. This is because these two potentials occur outside of the repassivation regime.

To summarize findings for resistance and capacitance of each treatment condition in each series, a simple ratio, R_a/R_b

R_b , was calculated for resistance after treatment over resistance before treatment. Such a ratio is presented for Series 1 and Series 2 in Fig. 9e, g, respectively. The ratio of capacitance after treatment over capacitance before treatment, C_a/C_b , is shown in Fig. 9f, h for Series 1 and Series 2, respectively.

For Series 1, as shown in Fig. 9e, the potential treatment with the lowest R_a/R_b ratio was +0.8 V, while the highest R_a/R_b ratio was associated with +0.7 V. In Fig. 9f, the treatment potential with the lowest C_a/C_b ratio was -0.4 V while the highest treatment potential occurred with +0.6 V for all protein concentrations.

For Series 2, after taking into consideration the ratio of resistance after to resistance before treatment along with the capacitance after treatment to capacitance before treatment, the potential that demonstrates the greatest anti-corrosion kinetics is +0.7 V. This is demonstrated by the larger R_a/R_b ratio for both electrolyte conditions. Although, +0.8 V in 30 g/L displays a R_a/R_b ratio as high as the R_a/R_b ratio for +0.7 V in 30 g/L protein, +0.8 and +0.6 V resulted in higher C_a/C_b ratios (Fig. 9h).

3.3 Surface Characterization Techniques

After using equivalent circuit modeling for Series 1 and Series 2, surface characterization techniques of WLI, SEM,

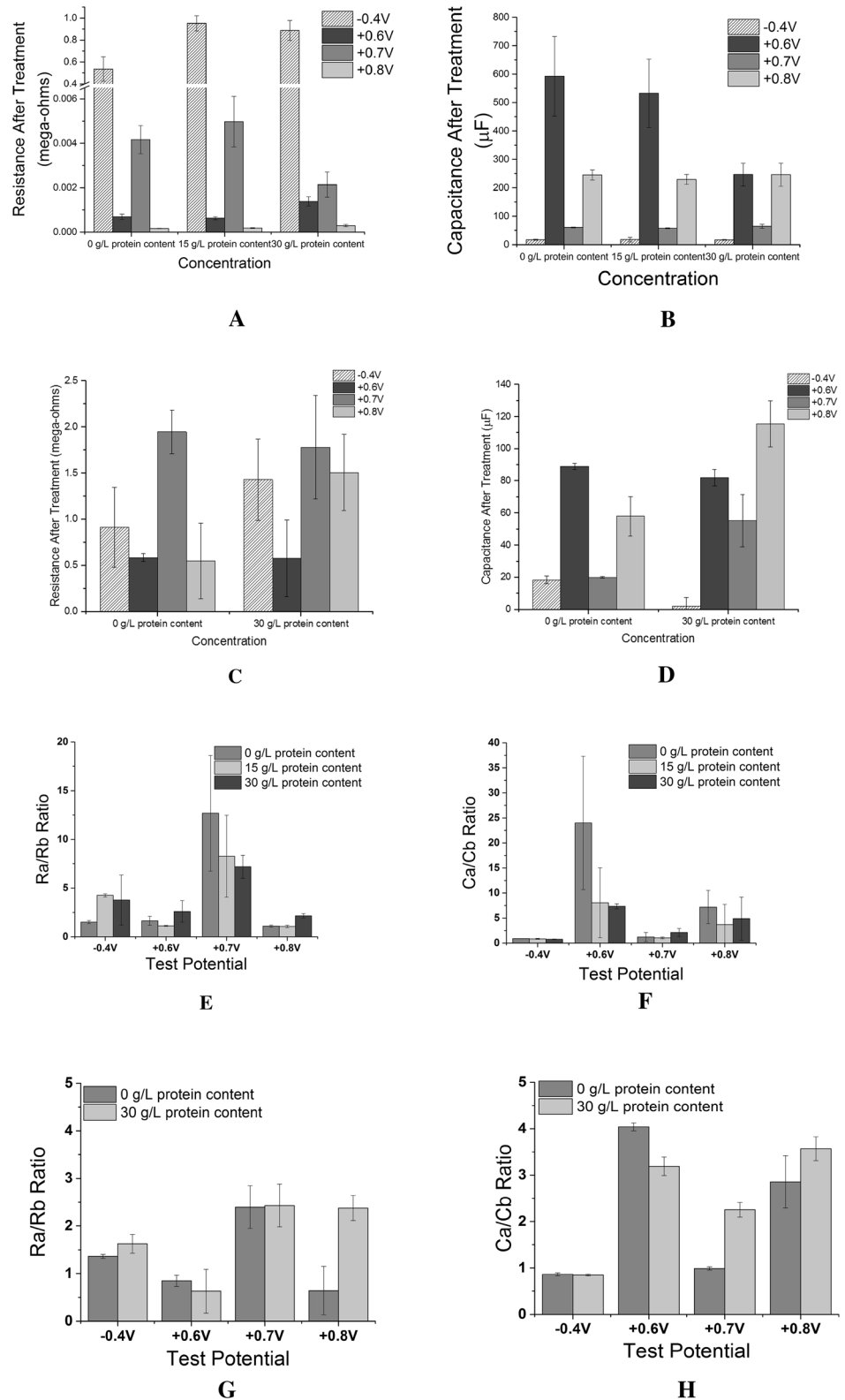
Fig. 9 a–h Resistance and capacitance after treatment and the ratios R_a/R_b and C_a/C_b for **a** series 1 and **b** series 2.

a Resistance after treatment in series 1 using 0, 15 and 30 g/L, protein content. **b** Capacitance after treatment in series 1 using 0, 15 and 30 g/L protein.

c Resistance after treatment in series 2 using 0 and 30 g/L protein content. **d** Capacitance after treatment in series 2 using 0 and 30 g/L protein content.

e Ratio of resistance after treatment over resistance before treatment in series 1. **f** Ratio of capacitance after treatment over capacitance before treatment in series 1. **g** Ratio of resistance after treatment over resistance before treatment in series 2.

h Ratio of capacitance after treatment over capacitance before treatment in series 2.



and Raman Spectroscopy were implemented to determine film characteristics.

3.3.1 Scanning Electron Microscopy (SEM) Images

The treated surfaces were examined using SEM, to understand film composition and surface homogeneity. The SEM images of all the samples are shown in Fig. 10a–m for the four treatment potentials in each of the electrolyte conditions (protein content: 0 and 30 g/L). There is no clear evidence of proteinaceous film formation at -0.4 and $+0.6$ V, Fig. 10a–e. Evidence of pitting is observed at $+0.7$ V at 0 g/L (Fig. 10e). At higher protein contents, of 15 and 30 g/L, there is evidence of proteinaceous film formation (Fig. 10f–j). The metal alloy appears with a lighter color while carbonaceous film formation is seen in the images as a darker shade. Similarly, the treated surfaces at $+0.8$ V also exhibit film formation, but not as intense as for $+0.7$ V. Electron-dispersive spectroscopy (EDS) was done for the sample surfaces to check the elemental composition of the film. The carbon-enriched film at $+0.7$ V and 30 g/L is evident from the EDS analysis (Fig. 11). Interestingly, EDS analysis shows the presence of elements (Mo) in the film, which possibly indicates a role for Mo+ in film formation (More explanations are included in a later section).

3.3.2 Raman Spectroscopy

Raman spectroscopy was done to understand and quantify the carbon that appears during EDS. This would help determine which treatment potential results in the higher carbon content film using potential treatments and 30 g/L protein content. Raman spectra were recorded in the range of 1100 – 1900 cm^{-1} . The typical collection was 30 s and the results reported were based on an average of 10–30 measurements. Raman spectroscopy results are shown in Fig. 12a–d. The samples that were chosen were for 30 g/L protein content at each treatment potential. Samples with this electrolyte condition were chosen because it was necessary to determine how protein would deposit on the alloy surface at each treatment potential. Previous work has shown the presence of a carbonaceous layer on retrieved articulating surfaces of MoM hip implants occurring at two peaks, 1383 and 1580 cm^{-1} , which are the D and G bands, respectively [7]. This carbonaceous layer, or tribofilm, has been suggested to help with limiting friction and protecting implant surfaces under in vivo conditions [19]. Figure 12c, d showed clear carbon D and G bands, similar to the graphitic carbon discovered in retrieved MoM hip replacements [19]. The treatments at -0.4 and $+0.6$ V did not produce the carbonaceous film as the D and G bands were absent on the Raman spectra. The spectra of samples

treated at -0.4 and $+0.6$ V are shown in Fig. 12a, b, respectively. Therefore, the potentials investigated in the present study indicate that $+0.7$ and $+0.8$ V result in two peaks which are a signature of the presence of the carbonaceous layer. It is interesting to note that $+0.7$ V (compared to $+0.8$ V) has a tenfold higher peak intensity of the carbonaceous layer. A higher peak may be indicative of more carbon content found within the film. Therefore, Raman spectroscopy results suggest that film seen for $+0.7$ V and 30 g/L protein has a higher intensity of carbon than $+0.8$ V and 30 g/L protein and any other condition we investigated.

4 Discussion

Based on our results, proteinaceous film formation is the result of interactions between the bulk alloy surface and the surrounding electrolyte under anodic treatment potentials. A treatment condition of key interest was $+0.7$ V and 30 g/L protein content since previous findings have indicated that applied potential of $+0.77$ V resulted in a proteinaceous deposition on CoCrMo thin film surfaces [20]. The treatment potentials induced corrosion of CoCrMo alloy in the form of pits and/or grain boundary corrosion. This resulted in metal ion exposure at the alloy surface, which using treatments of $+0.7$ and $+0.8$ V, may allow for bonding interactions to occur between the alloy and electrolyte content.

Our findings indicate that proteinaceous film formation occurs with potentials of $+0.7$ and $+0.8$ V. However, more proteinaceous film is formed at $+0.7$ than $+0.8$ V. This finding is not in agreement with Martin et al. [20], which leads us to believe that the properties of the CoCrMo alloy thin film are difficult to compare with the properties of the bulk CoCrMo alloy.

4.1 Mechanistic Behavior of Film Formation (Series 1)

By comparing the ratio of resistances (after treatment/before treatment) we could discern a trend with increased polarization resistance, comparing $+0.7$ to other treatment potentials. Interestingly, in Series 1 and Series 2, there was a decrease in polarization resistance with increasing protein concentrations, shown at a treatment potential of $+0.7$ V. This leads us to question the role of proteins in corrosion mitigation [21–24]. It appears that increasing protein content results in a decrease of polarization resistance, but at 15 g/L protein content there is an optimum amount of protein concentration for proteinaceous film formation to occur. However, what is important to understand is that the electrochemically treated film formation is to be placed

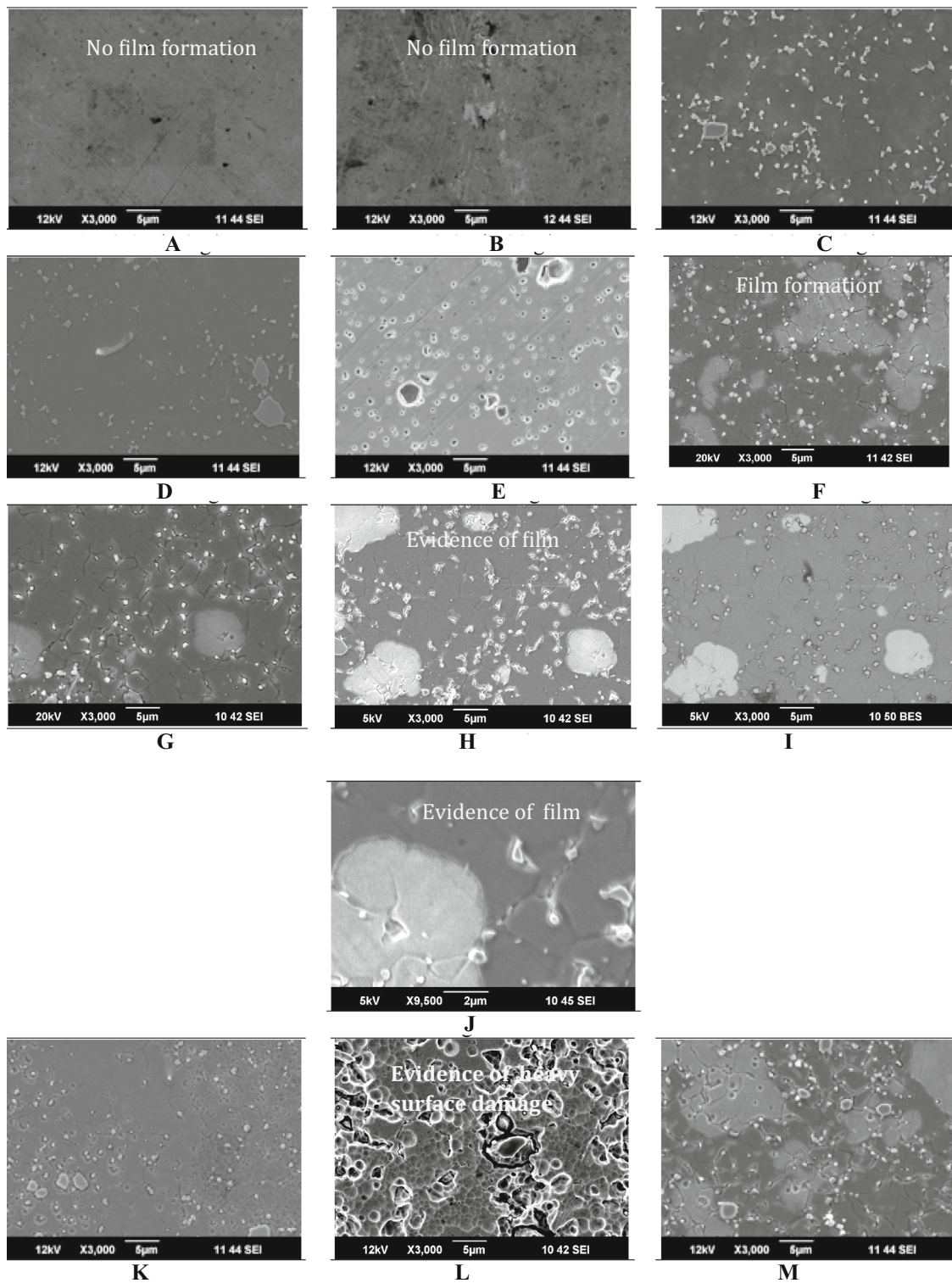
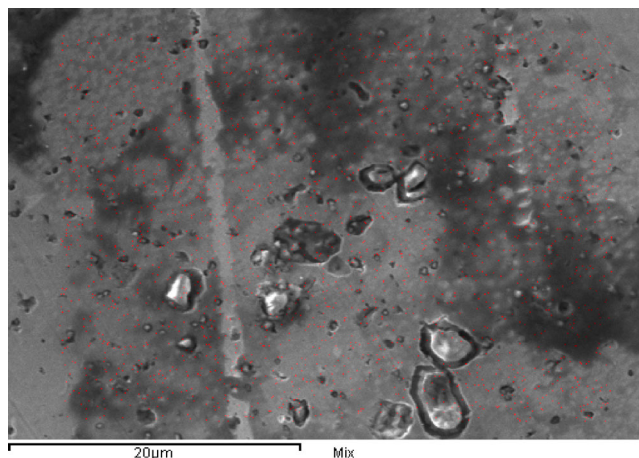


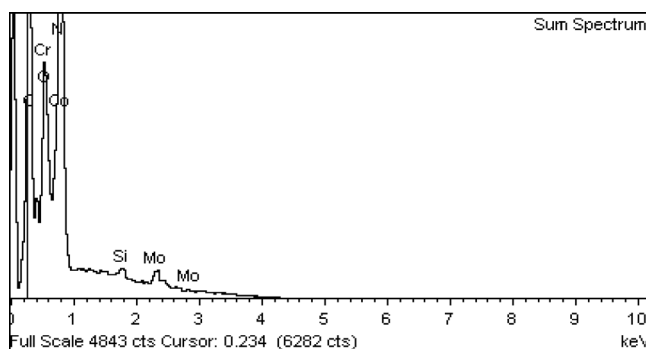
Fig. 10 a–m Scanning electron microscopy (SEM) images at various conditions. There is a clear evidence of film formation with +0.7 V group. **a** –0.4 V in 0 g/L, **b** –0.4 V in 30 g/L, **c** +0.6 V in 0 g/L, **d** +0.6 V in 30 g/L, **e** +0.7 V in 0 g/L, **f** +0.7 V in 15 g/L, **g** +0.7 V

in 30 g/L, **h** +0.7 V in 30 g/L-5 kV, **i** +0.7 V in 30 g/L-(back scattering image), **j** +0.7 V in 30 g/L, **k** +0.8 V in 0 g/L, **l** +0.8 V in 15 g/L, **m** +0.8 V in 30 g/L

Fig. 11 a, b EDS analysis of the electrochemically treated surface at +0.7 V and 30 g/L (protein content). The surface shows the presence of carbon around 15.31 weight %. The presence of Mo is also clear, which possibly indicates the role of Mo⁺ ion in the film formation



A



B

Element	Weight%	Atomic%
C K	15.31	43.97
O K	3.56	7.68
Si K	0.48	0.59
Cr L	19.38	12.86
Co L	55.71	32.61
Ni L	1.33	0.78
Mo L	4.22	1.52
Totals	100.00	

in vivo, and experimenting with the physiological potential is what will elucidate the role of proteinaceous film formation under in vivo settings, unlike the investigated treatment potentials, which were used to simply treat the alloy surface.

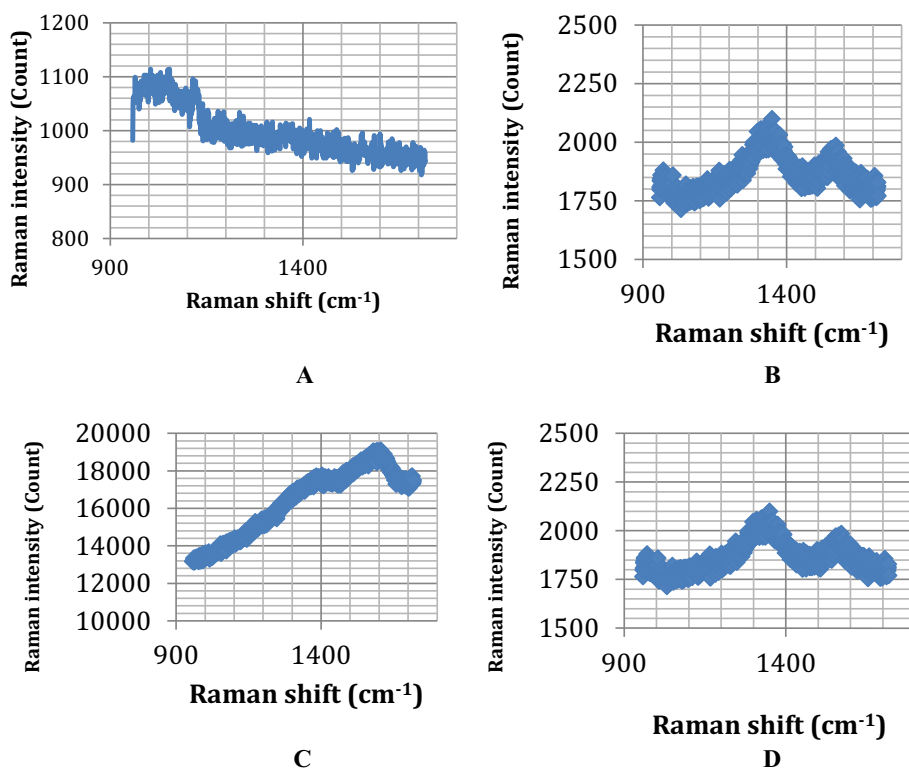
When comparing the ratio of capacitance after treatment to capacitance before treatment, it is evident that both treatment potentials of -0.4 and $+0.7$ V result in the lowest C_a/C_b ratio compared to $+0.6$ and $+0.8$ V. These findings are similar to those of Series 2 (some of the aspects), in which both -0.4 and $+0.7$ V resulted in lower C_a/C_b ratios.

4.2 Stability of the Film in the Clinically Relevant Conditions (Series 2)

Series 2 is clinically relevant as the EIS was conducted at an open circuit potential both before and after the treatment step (Step 5 of the electrochemical protocol), whereas in

Series 1 the EIS tests were conducted at the specific potential of the treatment potential. To determine the clinical stability in Series 2, the polarization resistance and the capacitance were determined after the treatment step. The results indicate that $+0.7$ V results in the highest overall resistance to corrosion compared to the other potentials. Additionally, it was shown that the capacitance associated with this anodic potential was the lowest compared to the other anodic potentials ($+0.6$ and $+0.8$ V). Although it was confirmed with Raman spectroscopy that both $+0.7$ and $+0.8$ V were able to elicit proteinaceous film formation, $+0.7$ V resulted in a larger Raman intensity of the graphitic carbon peaks than did $+0.8$ V. This suggests, moving forward with the prospect of film formation as a solution to MoM hip bearing contacts, that $+0.7$ V in proteinaceous electrolyte will likely be able to serve as a treatment potential, which will result in less corrosion of the contact surfaces (i.e., acetabular cup and femoral head) [25].

Fig. 12 a–d Raman spectroscopy images. The peaks at +0.7 and +0.8 V show the presence of graphitic carbon, as it was reported from tribolayer on retrieval implants. **a** -0.4 V, **b** +0.6 V, **c** +0.7 V, **d** +0.8 V



4.3 Possible Mechanisms of Film Formation

The proposed mechanism of film formation is shown in Fig. 13a–d. The precise mechanism for in vivo loading conditions and kinematics is still not well defined for the

generation of a tribolayer [26]. However, based on the parameters of this study, the formation of the film and film characteristics are influenced by, but are not limited to, the treatment potential. When corrosion and wear (tribocorrosion) processes occur, the CoCrMo alloy undergoes surface

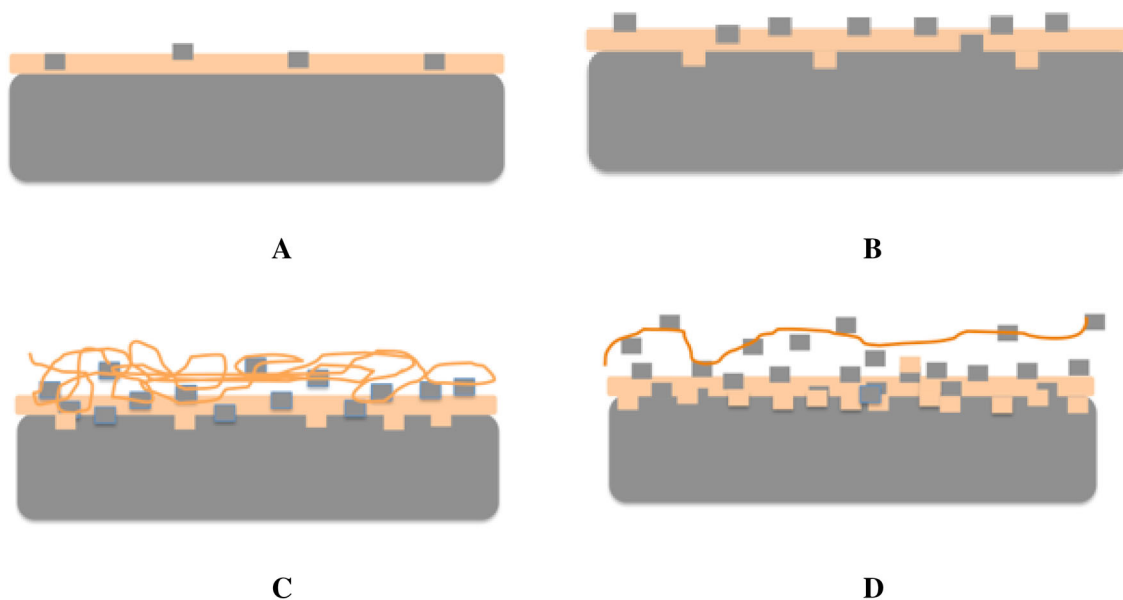


Fig. 13 a–d A schematic diagram shows film formation as a function of potential and protein concentration. The formed layer is composed of metal ions and decomposed proteins. The stability of the film is largely dependent on the potential at which the optimum amount (or

type) release of metal ions and the process of decomposition of protein are promoted. **a** -0.4 V in 30 g/L protein content, **b** +0.6 V in 30 g/L protein content, **c** +0.7 V in 30 g/L protein content, **d** +0.8 V in 30 g/L protein content

changes [27]. This means that exposed metal ions on the surface of the alloy are able to interact through bonding interactions with the surrounding environment, such as the synovial fluid because corrosion has caused the surface of the alloy to breakdown resulting in metal ion exposure. The bonding interactions between the exposed metal ions on the surface of the bulk alloy and the surrounding synovial fluid may result in a proteinaceous layer. This may be beneficial for protecting the implant surface from further corrosive processes *in vivo*. However, a treatment potential of -0.4 V did not result in any film formation. This can be seen in Fig. 12a, which has no film present. When comparing the anodic treatment potentials of $+0.6$, $+0.7$, and $+0.8$ V displayed in Figs. 13a–c, respectively, one sees an increase in metal ion release (gray squares). Potentials of $+0.6$ and $+0.8$ V, either resulted in too little or too much metal ion exposure and therefore had less film formation than did $+0.7$ V, as shown in the Raman spectra (Fig. 11). A potential treatment of $+0.6$ V did not display peaks of graphitic carbon under Raman spectroscopy, which may mean that no proteinaceous film formation occurred at this potential. A potential of $+0.7$ V appeared to result in a larger carbonaceous film than any other potential, which may be attributed to the number of metal ions that could bond to the components of the protein. After following the treatments at anodic/transpassive potentials, Raman spectroscopy and SEM with EDS demonstrated that film formation using 30 g/L protein content at $+0.7$ V results in a larger amount of carbon and a more homogenous surface compared to other treatment potentials. This phenomenon may have occurred because of an ideal amount of metal ion release, since exposing the alloy to potentials of $+0.6$ or $+0.8$ V may have caused too little or too much ion release, not allowing the protein film to form.

4.4 Schematic Diagram

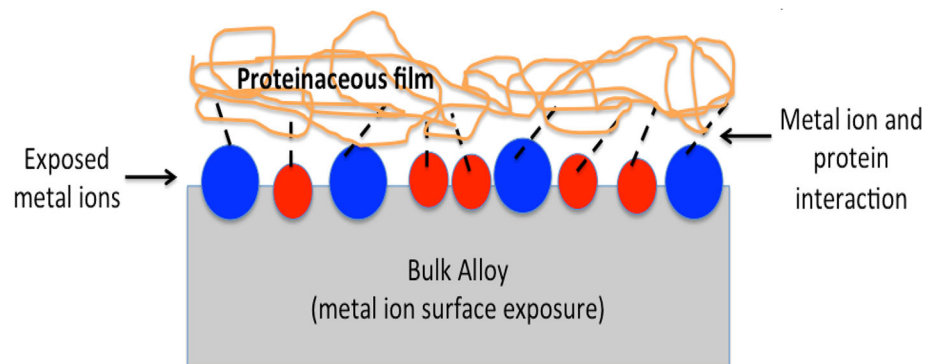
A proposed schematic of the film formation interaction is seen in Fig. 14 using proteinaceous electrolyte conditions based on the findings of the present study and of Martin

et al. [20]. The treatment potentials were able to induce CoCrMo corrosion in the form of pits and dissolution, resulting in metal ion exposure at the alloy surface, which allowed for bonding interactions to occur between the alloy and electrolyte [20]. However, protein film formation occurred only at potentials of $+0.7$ and $+0.8$ V. This suggests to the explanation that metal ions released during these two potentials were able to create in ideal conditions for the metal ions to interact and bond with protein constituents and thus allowing proteinaceous film formation on the alloy surfaces. It is still not understood which protein constituents are responsible for bonding interactions to take place. Additionally, at potentials of $+0.7$ and $+0.8$ V, a preferential dissolution of metal ions may be occurring. This phenomenon of preferential metal dissolution occurring at the various treatment potentials may influence the amount of proteinaceous film formation on the surfaces of the bulk alloy during the potentiostatic treatment step. The result is the formation of a distinct proteinaceous film at each potential.

4.5 Limitations, Future Scope, and Clinical Application

This study evaluated electrochemically induced film formation on CoCrMo alloy by varying protein concentration and treatment potential. Orthopedic implant longevity is of concern as *in vivo* corrosive processes may result in metal ion release into the body [28, 29]. The study also has its limitations: (1) There were only three protein concentrations that were used during the experiment: 0, 15, and 30 g/L, (2) and we only used one type of protein, albumin, which is found in BCS, (3) treatment potentials were varied in whole number increments; therefore, testing with smaller increments of $+0.05$ V may further increase precision, (4) in addition, a pH of 7.6 was used, as this is physiologically relevant. However, acidic and more basic pHs were not studied. (5) The circuit used for the EIS test (series 1), the inductive loops might be attributed to diffusional processes, occurring at the electrochemical double

Fig. 14 Proposed schematic diagram shows the interactions between the metal ions and the surrounding proteinaceous electrolyte. The chemistry and structure of the film are determined by such interaction and chemical bond formed between metal ions and decomposed proteins



layer. However, some sort of inductive characteristics can happen during the EIS test at high anodic potential, for instance, when pitting corrosion starts it generates a greater amount of current that will sum to the current measured due the small amplitude variation of potential during the EIS measurement. (6) Conducting XPS on sample surfaces will help characterize the adhered film deposition. (7) Additionally, it would be of interest to conduct mechanical testing of the samples to determine the dependence of the integrity of film formation on treatment potential and protein content [26, 29]. (8) The average thickness measurements of the film formed should also be taken into consideration. Further future investigations should include the utilization of additives in the electrolytic environment that induce tribofilm formation [18, 27].

Understanding the corrosion and wear mechanisms of hip joint implants will guide future design and functional needs of implants. Biological responses to metal debris are an area of pressing concern [30, 31]. Urgent attention is needed to deter the effects of MoM wear and corrosion [32–34]. Therefore, it would be of interest to conduct mechanical testing on the film samples under in vivo conditions and to analyze some parameters (i.e., load, contact area, contact type (conforming), and time) [35]. In addition, the present investigation adds to the knowledge of how proteins in the synovial fluid affect corrosion kinetics of implants.

5 Conclusions

In this study, we attempted to understand mechanistic aspects of carbonaceous film formation on CoCrMo alloy and its effectiveness at clinically relevant potentials. The following conclusions were made.

- The mechanistic study showed that the treatment potentials induced corrosion of CoCrMo alloy in the form of pits and/or grain boundary corrosion. This brings some concern on the mechanical stability of the film, particularly at subsurface level.
- An optimum level of metal ion release and the presence of specific state of decomposed protein is required for the film formation, indeed, this process determines the chemistry/nature of the film
- Based on the EIS resistance and capacitance data, it was identified that the electrochemical treatments at +0.7 V versus SCE (or very near values) will generate effective carbonaceous film than other treated potential.
- Although this study has shown that film formation may be able to limit CoCrMo alloy corrosion and its protective nature, further studies are still needed to evaluate its tribological/tribocorrosion behavior. Other parameters to investigate include pH levels of surrounding electrolyte solutions, loading/number of cycles during tribocorrosion testing, and other additives to understand the role of film formation in implant corrosion.

- Mechanical characterization is essential for the total understanding of the performance of the generated film. Further studies will be considered.

Acknowledgements NSF award-1160951 [Shull and Mathew (PIs)]. Allvac Inc. for the CoCrMo samples. Prof. Urban (Rush University) for the SEM facility.

References

1. Nwachukwu BU, Bozic KJ, Schairer WW, Bernstein JL, Jevsevar DS, Marx RG, Padgett DE (2015) Current status of cost utility analyses in total joint arthroplasty: a systematic review. *Clin Orthop Relat Res* 473(5):1815–1827
2. Kurtz S, Ong K, Lau E, Mowat F, Halpern M (2007) Projections of primary and revision hip and knee arthroplasty in the United States from 2005 to 2030. *J Bone Joint Surg* 89(4):780–785
3. Wyles CC, Jimenez-Almonte JH, Murad MH, Norambuena-Morales GA, Cabanela ME, Sierra RJ, Trousdale RT (2015) There are no differences in short- to mid-term survivorship among total hip-bearing surface options: a network meta-analysis. *Clin Orthop Relat Res* 473(6):2031–2041
4. Shetty V, Shitole B, Shetty G, Thakur H, Bhandari M (2011) Optimal bearing surfaces for total hip replacement in the young patient: a meta-analysis. *Int Orthop (SICOT)* 35(9):1281–1287
5. Dowson D (2001) New joints for the Millennium: wear control in total replacement hip joints. *Proc Inst Mech Eng [H]* 215(4):335–358
6. Calcerrada N, Fernández-Vega A, Valls-León C, Garcia-Cimbrello E (2016) Survey on the use and behaviour of metal-metal hip replacements in Spain. *Rev Esp Cir Ortop Traumatol* 60(1):20–28
7. Liao Y, Hoffman E, Wimmer M, Fischer A, Jacobs J, Marks L (2013) CoCrMo metal-on-metal hip replacements. *Phys Chem Chem Phys* 15(3):746–756
8. Liao Y et al (2012) New insights into hard phases of CoCrMo metal-on-metal hip replacements. *J Mech Behav Biomed Mater* 12:39–49
9. Sadiq K, Stack MM, Black RA (2015) Wear mapping of CoCrMo alloy in simulated bio-tribocorrosion conditions of a hip prosthesis bearing in calf serum solution. *Mater Sci Eng C* 49:452–462
10. Valero-Vidal C, Casabán-Julián L, Herraiz-Cardona I, Igual-Muñoz A (2013) Influence of carbides and microstructure of CoCrMo alloys on their metallic dissolution resistance. *Mater Sci Eng C* 33(8):4667–4676
11. Catelas I, Wimmer MA (2011) New insights into wear and biological effects of metal-on-metal bearings. *J Bone Joint Surg* 93(Supplement 2):76–83
12. Berry D, Abdel M, Callaghan J (2014) What are the current clinical issues in wear and tribocorrosion? *Clin Orthop Relat Res* 472(12):3659–3664
13. Mathew M, Jacobs J, Wimmer M (2012) Wear-corrosion synergism in a CoCrMo hip bearing alloy is influenced by proteins. *Clin Orthop Relat Res* 470(11):3109–3117

14. Yan Y, Yang H, Su Y, Qiao L (2016) Study of the tribocorrosion behaviors of albumin on a cobalt-based alloy using scanning Kelvin probe force microscopy and atomic force microscopy. *Electrochem Commun* 64:61–64
15. Souza MP, Lima L, Lima CP, Zavaglia CC, Freire CA (2009) Effects of pH on the electrochemical behaviour of titanium alloys for implant applications. *J Mater Sci Mater Med* 20(2):549–552
16. Shahgaldi B, Heatley F, Dewar A, Corrin B (1995) In vivo corrosion of cobalt-chromium and titanium wear particles. *J Bone Joint Surg* 77-B(6):962–966
17. Hesketh J, Ward M, Dowson D, Neville A (2014) The composition of tribofilms produced on metal-on-metal hip bearings. *Biomaterials* 35(7):2113–2119
18. Wimmer MA, Sprecher C, Hauert R, Täger G, Fischer A (2003) Tribochemical reaction on metal-on-metal hip joint bearings: a comparison between in vitro and in vivo results. *Wear* 255(7–12):1007–1014
19. Liao Y, Pourzal R, Wimmer MA, Jacobs JJ, Fischer A, Marks LD (2011) Graphitic tribological layers in metal-on-metal hip replacements. *Science* 334(6063):1687–1690
20. Martin EJ, Pourzal R, Mathew MT, Shull KR (2013) Dominant role of molybdenum in the electrochemical deposition of biological macromolecules on metallic surfaces. *Langmuir* 29(15):4813–4822
21. Guenther LE et al (2014) Biochemical analyses of human osteoarthritic and periprosthetic synovial fluid. *Proc Inst Mech Eng [H]* 228(2):127–139
22. Geringer J, Pellier J, Taylor ML, Macdonald DD (2013) Fretting corrosion with proteins: the role of organic coating on the synergistic mechanisms. *Thin Solid Films* 528:123–129
23. Martin EJ, Mathew MT, Shull KR (2015) Viscoelastic properties of electrochemically deposited protein/metal complexes. *Langmuir* 31(13):4008–4017
24. Valero Vidal C, Olmo Juan A, Igual Muñoz A (2010) Adsorption of bovine serum albumin on CoCrMo surface: effect of temperature and protein concentration. *Colloids Surf B Biointerfaces* 80(1):1–11
25. Hannemann F et al (2013) European multidisciplinary consensus statement on the use and monitoring of metal-on-metal bearings for total hip replacement and hip resurfacing. *Orthop Traumatol Surg Res* 99(3):263–271
26. Myant C, Cann P (2014) On the matter of synovial fluid lubrication: implications for metal-on-metal hip tribology. *J Mech Behav Biomed Mater* 34:338–348
27. Mathew MT, Wimmer MA (2013) 13-Tribocorrosion in artificial joints: in vitro testing and clinical implications. In: Yan Y (ed) *Bio-tribocorrosion in biomaterials and medical implants*. Woodhead Publishing, Sawston, pp 341–371
28. Mathew MT et al (2014) Tribolayer formation in a metal-on-metal (MoM) hip joint: an electrochemical investigation. *J Mech Behav Biomed Mater* 29:199–212
29. Afolaranmi GA, Akbar M, Brewer J, Grant MH (2012) Distribution of metal released from cobalt-chromium alloy orthopaedic wear particles implanted into air pouches in mice. *J Biomed Mater Res A* 100(6):1529–1538
30. Affatato S, Grillini L (2013) 1-Topography in bio-tribocorrosion. In: Yan Y (ed) *Bio-tribocorrosion in biomaterials and medical implants*. Woodhead Publishing, Sawston, pp 1a–22a
31. Whitehouse MR, Endo M, Masri BA (2013) Adverse local tissue reaction associated with a modular hip hemiarthroplasty. *Clin Orthop Relat Res* 471(12):4082–4086
32. Jacobs JJ et al (1995) Local and distant products from modularity. *Clin Orthop Relat Res* 319:94–105
33. Birkett N, El-Daly I, Ibraheim H, Mbubaegbu C (2015) Metallosis following full thickness wear in total hip arthroplasty. *J Surg Case Rep* 9:2015
34. Campbell P, Ebramzadeh E, Nelson S, Takamura K, Smet K, Amstutz HC (2010) Histological features of pseudotumor-like tissues from metal-on-metal hips. *Clin Orthop Relat Res* 468(9):2321–2327
35. Chang J-D (2014) Future Bearing surfaces in total hip arthroplasty. *Clin Orthop Surg* 6(1):110